Dynamical downscaling of future sea-level change in the western North Pacific using ROMS

Zhao-Jun Liu[1,2], Shoshiro Minobe[1], Yoshi N. Sasaki[1], and Mio Terada[1]

[1] *Department of Natural History Sciences, Graduate School of Science, Hokkaido University, Sapporo, Japan*

[2] *State Key Laboratory of Satellite Ocean Environment Dynamics, Second Institute of Oceanography, State Oceanic Administration, Hangzhou, China*

Corresponding author:
Zhao-Jun Liu
Phone: +86-571-86693289 Fax: +86-571-88839374
E-mail: zjliu@mail.sci.hokudai.ac.jp
Mail address: State Key Laboratory of Satellite Ocean Environment Dynamics,
Second Institute of Oceanography, State Oceanic Administration
36 Baochubei Road, Hangzhou, 310012, China

Abstract

The future regional sea level (RSL) rise in the western North Pacific is investigated by dynamical downscaling with the Regional Ocean Modeling System (ROMS) with an eddy-permitting resolution based on three global climate models—MIROC-ESM, CSIRO-Mk3.6.0, and GFDL-CM3—under the highest greenhouse-gas emission scenario. The historical run is forced by the air-sea fluxes calculated from Coordinated Ocean Reference Experiment version 2 (COREv2) data. Three future runs—ROMS-MIROC, ROMS-CSIRO, and ROMS-GFDL—are forced with an atmospheric field constructed by adding the difference between the climate model parameters for the 21st and 20th century to fields in the historical run.

In all downscaling, the RSL rise along the eastern coast of Japan is generally half or less of the RSL rise maxima off the eastern coast. The projected regional (total) sea level rises along the Honshu coast during 2081–2100 relative to 1981–2000 are 19–25 (98–104), 6–15 (71–80), and 8–14 (80–86) cm in ROMS-MIROC, ROMS-CSIRO, and ROMS-GFDL, respectively. The discrepancies of the RSL rise along the Honshu coast between the climate models and downscaling are less than 10 cm. The RSL changes in the Kuroshio Extension (KE) region in all downscaling simulations are related to the changes of KE (northward shift or intensification) with climate change.

Keywords

dynamical downscaling, regional sea level rise, western North Pacific, ROMS, CMIP5 climate models, global warming

1. Introduction

Sea level rise due to global warming is one of the most important changes that the oceans will undergo. Global mean sea level has risen at a rate of 3.2 ± 0.4 mm $year^{-1}$ over 1993–2012 based on satellite altimeter sea surface height (SSH) observations (Cazenave and Cozannet 2014). The recent Intergovernmental Panel on Climate Change (IPCC) Fifth Assessment Report (AR5) indicated that the global mean sea level rise in the 5% to 95% possibility range for the period 2081–2100 compared with 1986–2005 is likely to be 45 to 82 cm for the highest emission scenario Representative Concentration Pathway (RCP) 8.5 (Church et al. 2013).

Observational analysis (Bindoff et al. 2007; Cazenave and Cozannet 2014) and coupled climate models (Landerer et al. 2007; Yin et al. 2010; Yin 2012) indicate that sea level changes in response to a changing climate are not geographically uniform, and show substantial regionality. Based on the satellite records for 1993–2012, the sea level in the western tropical Pacific and eastern Indian Oceans increased much faster than the global mean. In the Atlantic, the sea level rose over the whole basin except for the Gulf Stream region in this period, whereas the sea level fell in the eastern tropical Pacific (Cazenave and Cozannet 2014). Using ensemble projections of 12 models of Coupled Model Intercomparison Project Phase 3 (CMIP3) under the Special Report on Emission Scenario A1B, Yin et al. (2010) calculated the dynamic sea level (sea level deviation from the geoid) during 2091–2100 relative to 1981–2000, and found dipole sea level rise patterns in the North Atlantic and North Pacific, and a belt-like pattern in the Southern Ocean. Furthermore, Yin (2012) analyzed 34 models of the Coupled Model Intercomparison Project Phase 5 (CMIP5) and found that there is overall consistency between the projections of regional sea level (RSL, the deviation of SSH from the global mean value) change by the end of the 21st century based on the CMIP5 and

CMIP3 models for similar scenarios. Major mechanisms for non-uniform dynamical sea level changes are surface wind changes and surface heat and freshwater flux changes. (Sakamoto et al. 2005; Sato et al. 2005; Lowe and Gregory 2006; Landerer et al. 2007; Yin et al. 2010; Suzuki and Ishii 2011a; Sueyoshi and Yasuda 2012; Zhang et al. 2014).

In response to global warming, the future sea level rise in the North Pacific will increase dramatically in the western subtropical gyre east of Japan (Yin et al. 2010; Yin 2012; Sueyoshi and Yasuda 2012). The large sea level rise is related to changes in the Kuroshio Extension (KE), which has a steep meridional sea level gradient, or to larger heat uptake of water masses. Sasaki et al. (2014) recently showed the large sea level variability in the KE region in relation to meridional shifts of the KE jet on decadal timescales, based on tide-gauge and satellite-derived SSH data. Using an atmosphere-ocean coupled climate model, Sakamoto et al. (2005) showed a large sea level rise south of the KE associated with the intensification of the KE in response to global warming. In contrast, Sato et al. (2006) showed a large sea level rise east of Japan associated with a poleward shift of the KE by using a North Pacific ocean general circulation model. Sueyoshi and Yasuda (2012) analyzed 15 CMIP3 models and found that some models exhibit a larger northward shift of the KE, and that others exhibit a greater intensification of the KE. They further suggested that different projected changes in the wind stress caused by changes in atmospheric circulations over the North Pacific result in different responses of the KE, which characterize the different patterns of RSL rise in the western North Pacific. Suzuki and Ishii (2011a) investigated sea level changes caused by CO_2-induced climate warming by using an atmosphere-ocean coupled climate model. They found that heat flux changes are more important than wind stress changes for the RSL rise in the southern recirculation of the KE in their model.

109 Suzuki and Ishii (2011b) decomposed baroclinic sea level changes based on the gridded
110 observational data set into vertical modes, and found that the global warming signals are
111 subducted into the ocean interior. This observation might be related to the formation of
112 the North Pacific subtropical mode water around the KE region and the southern
113 recirculation.

114 Japan is one of countries most likely to be affected by the sea level rise in the
115 western North Pacific caused by global warming (Hanson et al. 2011). The Organization
116 for Economic Co-operation and Development report (Nicholls et al. 2008) evaluated the
117 risk of coastal cities over the world for future coastal flooding, and the Japanese cities
118 Tokyo, Osaka-Kobe, and Nagoya are the 8^{th}, 13^{th}, and 17^{th} cities measured by assets
119 most exposed to coastal flooding in the 2070s, respectively. Therefore, there is a
120 practical need for projections of RSL change caused by climate change along the
121 Japanese coast.

122 However, the response of the Japanese coastal sea level to ocean circulation
123 changes caused by global warming has not yet been adequately studied. Current climate
124 models may not represent coastal sea level changes properly in the western North
125 Pacific because the model resolutions are too coarse to resolve the narrow western
126 boundary currents and the coastal topographies of islands. The most widely used
127 approach to solve this problem is dynamical downscaling, which has recently been
128 applied to projecting the effects of climate change on oceans (Meier 2006; Sato et al.
129 2006; Ådlandsvik 2008; Sun et al. 2012; Chamberlain et al. 2012; Liu et al. 2013;
130 Oliver et al. 2014; Seo et al. 2014; Liu et al. 2015). For example, Sato et al. (2006)
131 conducted dynamical downscaling to study global warming-induced changes in North
132 Pacific ocean circulations around Japan by using a North Pacific ocean general

133 circulation model driven by the sea surface flux derived from MRI-CGCM2.2, which is
134 a climate model contributing to CMIP3. Their model covers the domain 15°S–65°N and
135 100°E–75°W, with a horizontal resolution of 1/4° (zonally) and 1/6° (meridionally).
136 They reported that coastal sea level rise along Japan is 12–18 cm (including the global
137 mean thermal expansion of 10 cm, but ignoring land-ice melt etc.) from 2000 to 2070,
138 smaller than the 40 cm sea level rise off the east of Japan. However, the spatial
139 distribution of sea level changes along the Japanese coasts was not mentioned by Sato et
140 al. (2006). Moreover, because they did not choose the climate model to be downscaled
141 with a strategy for future sea level rise, it is not clear whether or not their results,
142 obtained from downscaling of only one climate model, are representative. Different
143 climate models produce different sea level changes (e.g., Sueyoshi and Yasuda 2012).
144 Seo et al. (2014) performed dynamical downscaling for the North Pacific marginal seas,
145 and thus their regional model covers the area 118°E–155°E and 18°N–50°N, which may
146 be suitable for these marginal seas but not for the western North Pacific to the east of
147 Japan. Therefore, downscaling of future RSL changes in the western North Pacific with
148 an appropriate strategy is required. In this study, we examine future Japanese coastal
149 RSL rise by dynamical downscaling with the Regional Ocean Modeling System
150 (ROMS) based on CMIP5 models outputs. For proper representation of western
151 boundary currents, which result from basin-scale atmospheric forcing, the ROMS
152 domain should cover the whole zonal extent of the North Pacific basin, which is much
153 wider than those in most previous downscaling studies (Meier 2006; Ådlandsvik 2008;
154 Sun et al. 2012; Chamberlain et al. 2012; Liu et al. 2013; Oliver et al. 2014; Seo et al.
155 2014; Liu et al. 2015). Dynamical downscaling involves a tradeoff between resolution
156 and number of experiments because of the limitation of computational resources.

157 Therefore, we conduct downscaling of three CMIP5 models, which are selected to
158 investigate the worst-case scenario. That is, we choose the three CMIP5 models that are
159 likely to show the largest RSL rise around Japan to evaluate the upper limits of sea level
160 rise.

161 The rest of the present paper is organized as follows. In Section 2, the CMIP5
162 models used for the downscaling are selected, and the main features of the models are
163 introduced. The methods used to generate the initial conditions, lateral boundary
164 conditions, and the atmospheric forcing fields required for the ROMS are described. In
165 Section 3, we compare the downscaled changes and those in the climate model
166 projections and examine the RSL changes around Japan by the end of the 21st century.
167 The summary and discussion are presented in Section 4.

168

169 ## 2. Methods and Data

170 ### 2.1 Global climate models

171 The CMIP5 climate model simulations used by the IPCC AR5 are mainly accessed
172 through the Program for Climate Model Diagnosis and Intercomparison (PCMDI,
173 website: http://cmip-pcmdi.llnl.gov/cmip5/). To project future climate change associated
174 with increasing concentrations of greenhouse gases, the CMIP5 climate models were
175 integrated under some RCP scenarios (Moss et al. 2010). To investigate the possible
176 large sea level rise in the western North Pacific, we focus our attention on the highest
177 emission scenario of RCP8.5 and climate models that have the highest RSL rise near
178 Japan. This strategy will provide the worst-case scenario of RSL rise. Figure 1 shows
179 the spatially averaged projected RSL change over a domain bounded by 25°N–40°N and
180 125°E–180°E for the 2081–2100 period relative to the 1981–2000 period for 33 CMIP5

models under the RCP8.5 scenario. RSL is evaluated in this study because we are interested in the regional expression of sea level rise. This domain is used for the average because the region shows significant sea level rise in the multi-model ensemble mean from 34 models (Yin 2012). We select the three models with the largest area-averaged RSL rise, which are the MIROC-ESM, the CSIRO-Mk3.6.0, and the GFDL-CM3, as base models for the future dynamical downscaling.

The major features of the three CMIP5 models are as follows. In the MIROC-ESM, the ocean component is the Center for Climate System Research (University of Tokyo) Ocean Component Model (COCO 3.4). The longitudinal grid spacing is about 1.4°, whereas the latitudinal grid intervals gradually vary from 0.5° at the equator to 1.7° near the North/South Poles (Watanabe et al. 2011). In CSIRO-Mk3.6.0, the ocean component is the Modular Ocean Model (MOM 2.2) with a horizontal resolution of 1.875° × 0.9375° (Rotstayn et al. 2010; Jeffrey et al. 2013). The ocean model component of the GFDL-CM3 uses MOM4p1 code. The ocean model resolution is 1° for longitude. The meridional resolution gradually transitions from 1/3° at the equator to 1° at 30°N and remains as 1° between 30°N and 65°N in the Arctic (Griffies et al. 2005; Griffies et al. 2011).

2.2 Regional ocean model

The present study uses ROMS to downscale and project sea level changes caused by climate change dynamically. The ROMS can be used for a diverse range of applications from local to planetary scales (e.g., Curchiser et al. 2005; Seo et al. 2007; Ådlandsvik 2008; Lorenzo et al. 2008; Han et al. 2009; Seo et al. 2014). The model solves the incompressible and hydrostatic primitive equations, and uses a free sea

surface on horizontally curvilinear coordinates and generalized terrain-following sigma vertical coordinates (Haidvogel et al. 2000; Shchepetkin and McWilliams 2005).

The model domain covers almost the entire North Pacific basin (110°E–100°W, 5°N–50°N) with an eddy-permitting 0.25° × 0.25° horizontal resolution and 32 sigma levels in the vertical direction. The eddy-permitting model has biases, such as the Kuroshio Current overshooting northward along eastern coast of Japan (Shu et al. 2013) and northward shift of the KE (Sumata et al. 2012). Therefore, we examine biases in the model compared with observations, as described in Section 3.1, and consider the biases in interpreting the downscaled results.

Schemes used for boundary conditions and mixing are as follows. The radiation lateral boundary condition with nudging (time scale of 30-day) is used for temperature and salinity along the open boundaries at 5°N, 50°N, 110°E, and 100°W that permit long-term stable integration (Seo et al. 2007). A wall boundary condition is chosen for the sea surface elevation and the normal velocity. This is a zero gradient condition for surface elevation and zero flow for the normal velocity (Marchesiello et al. 2001). Harmonic horizontal mixing along an epineutral (constant density) surface is applied to the tracers, whereas biharmonic horizontal mixing along constant sigma surfaces is applied to the momentum. A third-order upstream horizontal advection scheme and fourth-order centered vertical advection scheme for momentum and tracer equations are used (Shchepetkin and McWilliams 2005). K-profile turbulence closure (Large et al. 1994) is used for vertical mixing, and quadratic drag is applied to the bottom friction.

2.3 ROMS experiment settings

a. Historical run (1951–2000)

229 The historical run (ROMS-Hist) for the period 1951–2000 provides a reference for
230 interpreting future run results. Initial salinity and potential temperature are set as the
231 climatology of the World Ocean Atlas 2009 (WOA2009) (Locarnini et al. 2010;
232 Antonov et al. 2010), and the initial sea level and velocities are set to zero. At the
233 surface, the historical run is forced with six-hourly winds, air temperature, sea level
234 pressure, specific humidity, daily mean downward shortwave and downward longwave
235 radiation of the Coordinated Ocean Reference Experiment version 2 (COREv2) (Large
236 and Yeager 2009) from 1951 to 2000. The primary data source of COREv2 data set is
237 the NCEP/NCAR R1 reanalysis product, climatological biases in NCEP/NCAR R1 have
238 been corrected in COREv2 on the basis of comparison with more reliable satellite and
239 in situ measurements (Large and Yeager 2009). The effective ocean albedo is set to
240 0.065 uniformly in the model domain, which is in the appropriate range of this domain.
241 Upward longwave radiation is dependent on simulated sea surface temperature (SST).
242 Surface wind stress and net heat fluxes are computed by using a bulk formula (Fairall et
243 al. 2003). The model sea surface salinity is restored to the climatology values of CORE
244 v2 data with a 30-day period. The lateral boundary values are provided from monthly
245 mean Simple Ocean Data Assimilation version 2.2.4 (SODA 2.2.4) in the period from
246 1951 to 2000 (Carton and Giese 2008).
247
248 b. Future run (2051–2100)
249 Because CMIP5 models have biases in parameters that are used for momentum and
250 heat flux calculations in downscaling in the present climate (Lee et al. 2013), the future
251 run in the late 21st century is forced with atmospheric fields constructed by adding the
252 monthly mean difference between the CMIP5 model parameters from the 21st and 20th

century to the observed parameters, which are mostly six-hourly, in the 20th century. The details of the approach are as follows. First, we calculate the monthly mean changes between 2051–2100 (RCP8.5) and 1951–2000 (CMIP5 historical) in each month and set of years (e.g., April 2079 minus April 1979) for the simulated winds, air temperature, relative humidity, sea level pressure, net shortwave and downward longwave radiation. Upward longwave radiation is dependent on simulated SST. Secondly, these monthly mean changes are added to CORE v2 atmospheric surface fields for the corresponding month and year for the 1951–2000 period used for ROMS-Hist. Finally, the bulk formula is used to calculate the projected surface fluxes of momentum, and sensible and latent heat, with the parameters determined in the second step. Similarly, the model sea surface salinity at each grid point is restored to the value that is given by the climatology used for historical run added 50-year time series of monthly sea surface salinity differences between 2051-2100 period and 1951-2000 period. We also apply this approach to the initial and lateral boundary conditions. The initial conditions for the future runs are also generated by adding the changes in temperature and salinity between January 1951 and January 2051 in the CMIP5 models to the initial condition of ROMS-Hist. The initial sea level and velocities are set to zero in all future runs. The lateral boundary conditions for the future runs are created by adding changes in monthly mean temperature, salinity, and velocity between 2051–2100 and 1951–2000 in the CMIP5 models to the respective fields in SODA 2.2.4 in the period 1951–2000. We call the three ROMS future runs forced by the MIROC-ESM, CSIRO-Mk3.6.0, and GFDL-CM3 variables ROMS-MIROC, ROMS-CSIRO, and ROMS-GFDL, respectively. The last 20 years of the historical run and of all future runs are used in the following analyses.

277

278 2.4 Regional sea level

279 To focus on the regional distribution, we analyze RSL, which is the sea level at
280 each grid point minus the global mean (e.g., Yin et al. 2010; Zhang et al. 2014). The
281 RSL in the CMIP5 models is given by

282 $$h'_{CM}(x,y,t) = h_{CM}(x,y,t) - \bar{h}^{G}_{CM}(t) \quad (1)$$

283 where h_{CM} is the sea level in a climate model (zos in CMIP5), $\bar{h}^{G}_{CM}$ is the global mean
284 sea level, *t* is time, and *x* and *y* are the zonal and meridional coordinates, respectively.
285 Because the ROMS domain does not cover the global, the RSL in ROMS simulations is
286 defined by

287 $$h'_{ROMS}(x,y,t) = h_{ROMS}(x,y,t) - \bar{h}^{G}_{CM}(t) - (\bar{h}^{D}_{ROMS}(t) - \bar{h}^{D}_{CM}(t)) \quad (2)$$

288 where the h_{ROMS} is the sea level output of ROMS, $\bar{h}^{G}_{CM}$ is the corresponding CMIP5
289 model's global mean, $\bar{h}^{D}_{ROMS}$ and $\bar{h}^{D}_{CM}$ are the means over the current model domain
290 (110°E–100°W, 5°N–50°N) in ROMS and the CMIP5 models, respectively.

291

292 2.5 Observational data

293 The ROMS-Hist is compared with the following observational data. The maps of
294 weekly absolute dynamic height are compiled from the TOPEX/Poseidon, ERS-1/2,
295 Jason-1, and Envisat altimeter observations on a 1/3°× 1/3° Mercator spatial resolution
296 grid from January 1993 to December 2000, distributed by the Archiving, Validation and
297 Interpretation of Satellite Oceanographic Data (AVISO) (Ducet et al. 2000). The
298 absolute dynamic height products are computed with consistent sea level anomaly and
299 mean dynamic topography field (Rio and Hernandez 2004).

300

301 # 3. Results

302 ## 3.1 Comparison of ROMS-Hist and observations

303 To evaluate the capability of the ROMS downscaling, the time-mean surface
304 velocity obtained from the three CMIP5 models, ROMS-Hist, and satellite data are
305 compared in Figure 3. Generally, all three CMIP5 models show a broad, weak Kuroshio
306 Current and KE. It should be noted that ROMS-Hist fails to produce some observed
307 features, as expected for an eddy-permitting model (e.g., Kagimoto and Yamagata 1997;
308 Sumata et al. 2012; Shu et al. 2013). The KE is mainly formed roughly along 37°N with
309 a minor eastward flow around 30°N. In the satellite observations, the Kuroshio Current
310 separates from the coast and turns into the KE around 35°N. The modeled extension
311 around 30°N is associated with the separation of the Kuroshio Current from the coast to
312 the east of Kyushu. The systematic discrepancies between the ROMS-Hist and the
313 observations should be considered in interpreting downscaled future changes.

314 The different surface current structures among the CMIP5 climate models,
315 ROMS-Hist, and observation are reflected in differences in SSH, because the SSH
316 gradient is closely related to the surface current speeds through the geostrophy. Figure 4
317 shows that ROMS-Hist exhibits sharp SSH gradients across the Kuroshio Current and
318 the KE as observed, although the CMIP5 climate models have broad, weak gradients
319 especially over the KE. Proper reproduction of sharp SSH gradients is important in sea
320 level changes, because shifts in SSH fronts can produce large sea level changes.

321 Another deficiency in the CMIP5 climate models is that the three straits connecting
322 the Japan Sea either to the North Pacific Ocean or to marginal seas, such as the
323 Tsushima, Tsugaru, and Soya Straits (Fig. 2), are not properly resolved. The Tsugaru

Strait is closed in MIROC-ESM and CSIRO-Mk3.6.0, whereas the Soya Strait is closed in GFDL-CM3. Therefore, examination of future flow changes through the straits is impossible using these climate models, but is possible using ROMS downscaling. The observed volume transports are 2.6 Sv (1 Sv = 10^6 $m^3 s^{-1}$) (Fukudome et al. 2010), 1.6 Sv (Ito et al. 2003), and 0.7 Sv (Fukamachi et al. 2010) through the Tsushima, Tsugaru, and Soya Straits, respectively, whereas they are 2.6, 2.4, and 0.2 Sv in ROMS-Hist (Fig. 15). Hence, ROMS-Hist represents the Tsushima Strait throughflow very well, whereas overestimates the Tsugaru Strait and underestimates the Soya Strait throughflow.

3.2 Regional sea level changes around Japan

In this section, we investigate how large the RSL changes around Japan are by the end of 21st century under the RCP8.5 scenario. Figure 5 shows the projected changes in mean RSL around Japan during 2081–2100 relative to 1981–2100 in the three CMIP5 models and in the corresponding ROMS downscaling simulations. The three CMIP5 models project RSL rises in the subtropical gyre east of Japan, with a maximal RSL rise of 44, 37, and 27 cm in MIROC-ESM, CSIRO-Mk3.6.0, and GFDL-CM3, respectively.

The RSL changes in the ROMS simulations have finer structures and higher magnitudes than those in the CMIP5 models, with some similarities among different downscaling simulations (Fig. 5). The ROMS downscaling exhibits larger RSL rise maxima than the CMIP5 models; the RSL rise maxima reach 63, 67, and 76 cm in ROMS-MIROC, ROMS-CSIRO, and ROMS-GFDL, respectively. The downscaled RSLs commonly exhibit zonally aligned three maxima along 37°N between 140°E and 160°E. A comparison of these RSL rise patterns with the surface currents at the end of the 21st century (Fig. 6) and the end of the 20th century (Fig. 3) reveals that the RSL rise

348 along 37°N is associated with the northward shift of the KE in ROMS-MIROC and
349 ROMS-GFDL. The relatively large RSL rise at 30°N and 40°N is related to the
350 substantial weakening of the eastward current along 30°N found in ROMS-Hist and to
351 the increased eastward currents around 40°N. It should be noted that in all ROMS
352 simulations, RSL increases larger than 30 cm are limited to seaward of the continental
353 shelf off the Japanese archipelago, so that the high off-shore RSL rise would not reach
354 the coast of Japan.

355 To better understand the relationship between the off-shore and coastal RSL
356 changes, we examine the meridional distribution of the RSL rise zonally averaged over
357 145°E–155°E and that on the Japanese eastern coast simulated by the CMIP5 models
358 (Fig. 7) and the ROMS downscaling (Fig. 8). We select the coastal RSL as the RSL at
359 the ocean grid located next to the easternmost land grid of Japan at each latitude. In all
360 CMIP5 models and ROMS simulations, the RSL changes along the eastern coast of
361 Japan are generally half or less of the RSL rise maxima off the eastern coast of Japan.

362 Figure 9 shows RSL rises at all coastal grid points along Honshu Island, which is
363 artificially connected to Kyushu and Shikoku islands forming one island in the ROMS
364 simulations (Fig. 2), and Hokkaido Island. The coastal RSL changes during 2081–2100
365 relative to 1981–2000 derived directly from the three CMIP5 models and those obtained
366 from ROMS downscaling are shown in Figs. 9a and 9b for the eastern and western
367 coasts, respectively. The projected RSL rises during 2081–2100 relative to 1981–2000
368 along Honshu are 19–25, 6–15, and 8–14 cm in ROMS-MIROC, ROMS-CSIRO, and
369 ROMS-GFDL, respectively. An important feature is that the differences in RSL changes
370 between downscaling simulations and the corresponding CMIP5 models are less than 10
371 cm along Honshu coast. This means that if a 10 cm discrepancy is allowed at the

maximum, we can use climate model outputs directly to assess the RSL rise along Honshu coast. The smaller differences in coastal RSL than in off-shore RSL between the ROMS downscaling and climate models are probably caused by coastally trapped shelf waves. These waves tend to average sea level along the coast, resulting in roughly constant coastal sea level, which is given by the average of sea level at the northern and southern ends of the island (Liu et al. 1999). Tsujino et al., (2008) successfully obtained semi-analytical solution of coastal sea-level around Japan arising through adjustment of coastal trapped waves and Rossby waves consistent with their OGCM of similar grid-spacing from the present model. We compared the simulated coastal sea levels and observed sea level anomalies averaged over 4 stations, which were selected by Japan Meteorological Agency for the most reliable long available stations, along the Japanese coast in the period of 1971–2000 (r=0.37, significant at the 95% confidence level). Therefore, the year-to-year variability of the model coastal sea level is consistent with that in the observed sea levels along the Japanese coast. The northward decrease in RSL changes on the western Honshu coast may be consistent with the northward propagation of shelf waves with damping along the route.

Although the RSL rises in the CMIP5 models and in ROMS downscaling are generally similar along Honshu, they can be substantially different at the islands separated from Honshu, because sea levels at those islands are not affected by the averaging effects of coastal waves. Here, we examine sea level change at Okinawa Island (Fig. 2), because extremely high sea levels have occurred there (Tokeshi and Yanagi 2003), suggesting that it is important to project the RSL rise at Okinawa Island in the future warming climate. Although Okinawa Island is too small to be represented as an island in the current ROMS downscaling simulations, sea level changes at the

island would be well approximated by the modeled sea level changes at that location. Figure 10 shows the projected RSL changes at Okinawa Island during 2081–2100 relative to 1981–2000 in the three CMIP5 models and corresponding ROMS simulations. Both ROMS-MIROC and ROMS-CSIRO project high RSL rises at Okinawa Island of 29 and 32 cm, respectively, which are as much as or larger than the RSL rise maxima on the Honshu coast. However, ROMS-GFDL projects relatively small RSL rise at Okinawa Island of 9 cm. The difference between CSIRO-Mk3.6.0 and ROMS-CSIRO is 16 cm, exceeding the aforementioned maximal discrepancy of 10 cm along Honshu coast between the CMIP5 climate model and ROMS downscaling.

3.3 Three-dimensional oceanic changes

As revealed by previous studies, the spatial distributions of RSL rise in the western North Pacific are related to the upper ocean changes (Sakamoto et al. 2005; Sato et al. 2006; Suzuki and Ishii 2011a; Sueyoshi and Yasuda 2012). In this section, we investigate future changes below the surface in the western North Pacific to understand the relationships between these changes and the RSL rise around Japan.

Sea level changes accompanied by density changes are represented by dynamic height (DH). DH is a commonly used parameter that can be calculated in terms of temperature and salinity by Eq. 3 (Gill 1982) with reference to 2000 dbar.

$$\Delta DH = \frac{1}{g}\int_{2000}^{0}(v_s(S,T,p) - v_s(35\ psu, 0\ ℃, p))dp \quad (3)$$

Here, S is salinity, T is temperature, g is acceleration due to gravity, and v_s is specific volume, given by the reciprocal of in situ density, and the anomaly of specific volume is defined as the specific volume related to that at the same pressure for salinity of 35 psu and temperature of 0 °C. Thus, DH is defined as the vertical integration of the specific

volume anomaly from the pressure of 2000 to 0 dbar (at the surface). For consistency with the RSL rise, regional dynamic height (RDH) is defined in a similar manner to the RSL definition (Eq. 2) as

$$\Delta DH'_{ROMS} = \Delta DH_{ROMS} - \Delta\overline{DH}^{G}_{CM} - (\overline{\Delta DH}^{D}_{ROMS} - \overline{DH}^{D}_{CM}) \quad (4)$$

where the ΔDH_{ROMS} is DH calculated by the ROMS outputs, $\overline{\Delta DH}^{G}_{CM}$ is the corresponding CMIP5 model's global mean DH, $\overline{\Delta DH}^{D}_{ROMS}$ and $\overline{\Delta DH}^{D}_{CM}$ are the DH means over the North Pacific ROMS domain in ROMS and the CMIP5 models, respectively.

Figure 11 shows the RDH changes during 2081–2100 relative to 1981–2000 obtained from the three ROMS downscaling simulations. The comparison of the RDH changes (Figs. 11(a)–(c)) and RSL rises (Figs. 5(d)–(f)) indicate that the RDH changes very well reproduce the major features of RSL rises described in the previous section, including RSL rises associated with the KE changes.

We examine subsurface signatures related to RSL rises penetrate downward. Figure 12 shows projected changes in mean eastward velocity zonally averaged from 145°E to 155°E in a meridional-vertical cross section across the KE during 2081–2100 relative to 1981–2000 in the ROMS simulations. The zonal velocity changes are consistent with the aforementioned KE changes. Velocity increase in ROMS-CSIRO is collocated with the KE in the 20th century, indicating the KE intensification. In ROMS-GFDL, velocity increases (decreases) to the north (south) of the KE axis in the 20th century, showing the northward migration of the KE axis. In ROMS-MIROC, strong velocity increase is found to the north of the 20th century KE axis but weak increase occur almost over the whole KE axis, suggestive of the combination of the northward migration and overall intensification. The zonal velocity changes mainly occur in the upper 1000 m, and

444 penetrate down to 2000 m in ROMS-GFDL. The vertical penetration may suggest that
445 this pattern is unlikely to be caused by heat or fresh water fluxes at the surface. This is
446 because such thermohaline flux changes would cause temperature and salinity changes
447 primarily limited to major water masses such as subtropical mode water at depths of
448 300–400 m or shallower (Suzuki and Ishii 2011b). Therefore, these changes are
449 probably forced by wind stress changes (e.g., Sakamoto et al. 2005; Sato et al. 2006;
450 Sueyoshi and Yasuda 2012). The velocity changes in ROMS-MIROC and
451 ROMS-CSIRO penetrate to a shallower depth than ROMS-GFDL. In addition, in
452 ROMS-CSIRO, near surface decrease of density is much more prominent than in the
453 other two models (not shown). These features in ROMS-CSIRO suggest that water mass
454 changes may play a more important role in the RSL in this model than in the others,
455 while both the effects of wind stress changes and water mass changes are all included in
456 ROMS-MIROC. Temperature changes penetrate to 2000 m, which is consistent with the
457 zonal velocity changes of the KE (Fig. 13), whereas the vertical penetration of the
458 salinity changes are limited to the upper 1000 m because of the lack of mean salinity
459 gradients deeper than 1000 m (not shown). All ROMS simulations commonly show that
460 the positive Sverdrup function changes east of Japan (Fig. 14) are caused by the
461 negative wind stress curl changes over the North Pacific (not shown).

462 The RDH changes shown in Figs. 11(a)–(c) are decomposed into thermosteric and
463 halosteric components. The decomposition methods are described in Eqs. (5) and (6)
464 (Landerer et al. 2007; Zhang et al. 2014).

465 $$\Delta DH_T = \frac{1}{g}\int_{2000}^{0}(v_s(35psu, T, p) - v_s(35\ psu, 0\ ℃, p))dp \quad (5)$$

466 $$\Delta DH_S = \frac{1}{g}\int_{2000}^{0}(v_s(S, 0\ ℃, p) - v_s(35\ psu, 0\ ℃, p))dp \quad (6)$$

467 Here, ΔDH_T and ΔDH_S are the thermosteric and halosteric DH, respectively. The
468 calculation of regional thermosteric and halosteric DH is similar to that of RDH given
469 in Eq. (4). Figures 11(d)–(f) and 11(g)–(i) show the regional thermosteric and halosteric
470 contributions, respectively, to RDH changes during 2081–2100 relative to 1981–2000.
471 The sum of these two components recover the RDH changes well (Figs. 11(j)–(l)). Thus,
472 although the density is a nonlinear function of temperature, salinity and depth, its
473 nonlinearity is weak with respect to temperature and salinity differences caused by the
474 climate change. In all ROMS simulations, thermosteric components dominate the RDH
475 change between 30°N and 40°N. Smaller halosteric components contribute to producing
476 a larger RDH to the south than to the north. Consequently, the thermosteric component
477 gives the major RDH, and thus the major RSL rise features, whereas the effect of
478 halosteric component is small.

479 The spatial structure of the sea level changes may be associated with changes in the
480 throughflow transport via the Tsugaru, Tsushima, and Soya Straits, because differences
481 in sea level between the upstream and downstream of a strait strongly constrains
482 throughflows (Ohshima 1994; Lyu and Kim 2005; Tsujino et al. 2008). Figure 15 shows
483 the time-mean volume transports during 1981–2000 period and 2081–2100 period
484 through the Tsushima, Tsugaru, and Soya Straits in ROMS downscaling. All transports
485 through the straits will increase in the future warming climate. ROMS-CSIRO projects a
486 much larger increase in the transports of each strait compared with the other two
487 downscaling simulations. This is probably because ROMS-CSIRO projects a negative
488 RSL rise in the subpolar gyre (Fig. 5), in contrast to the positive RSL rise in the other
489 two models. The negative RSL rise in the subpolar gyre, combined with the positive
490 RSL rise in the subtropical gyre is associated with the larger increase in SSH difference

491 between the subpolar and subtropical gyres in ROMS-CSIRO than in other two models.

492 Apart from the context of sea level rise, an interesting parameter in ROMS
493 downscaling is SST, which is important in feedback from the ocean to the atmosphere
494 (e.g., Small et al. 2008; Chelton and Xie 2010) and marine ecosystems (e.g.,
495 Abdul-Aziz et al. 2011). Figures 16 (a)–(c) show that the three climate models exhibit
496 the maximal SST increase to the east of the Tsugaru Strait, which suggests that the
497 northward migration of the Kuroshio Current affects these models. The maximal SST
498 warming in ROMS downscaling is reminiscent of the SST change in the climate model
499 (Figs. 16(d)–(f)), as downscaling simulations also have maximal SST warming just east
500 of the Tsugaru Strait. However, the magnitude of the maximal SST warming in
501 ROMS-GFDL is as high as 11 °C, nearly 1.2 times larger than that in the corresponding
502 climate model (9 °C). In addition, ROMS-CSIRO exhibits enhanced SST warming
503 relative to the climate model, whereas maximal SST warming in ROMS-MIROC is only
504 slightly larger than in the climate model. The localized maximal SST change is probably
505 related to the larger northward intrusion of the Kuroshio Current at the end of the 21st
506 century than that at the end of the 20th century in surface current velocities (Figs. 3 and
507 6). The present downscaling model has a bias in the separation latitude of the Kuroshio
508 Current from the eastern coast of Japan. However, the maximal SST increase around the
509 northernmost latitude of the coastal Kuroshio Current in climate models and ROMS
510 downscaling simulations suggests that future changes in the Kuroshio Current may
511 result in large SST change around its separation latitude observed at about 35°N.

512

513 ## 4. Summary and discussion

514 We investigated the future RSL rise in the western North Pacific by conducting

515 dynamical downscaling by using ROMS with eddy-permitting 0.25° × 0.25° resolution.
516 To evaluate the worst cases of RSL rise at the end of 21st century around Japan, we
517 selected three climate models that have the highest RSL rise near Japan (Fig. 1),
518 MIROC-ESM, CSIRO-Mk3.6.0, and GFDL-CM3, under the highest greenhouse-gas
519 emission scenario, RCP8.5. The dynamical downscaling are performed for two epochs:
520 the historical run (1950–2000) and the future run (2051–2100). The historical run,
521 ROMS-Hist, is forced by the air-sea fluxes calculated by using COREv2 data. Three
522 future runs—ROMS-MIROC, ROMS-CSIRO, and ROMS-GFDL—are forced with an
523 atmospheric field constructed by adding the difference between the CMIP5 parameters
524 of the 21st and 20th century to the present forcing fields used in ROMS-Hist.

525 The ROMS downscaling captures finer structures and stronger magnitudes for the
526 RSL changes than those in the CMIP5 models. The downscaled changes commonly
527 exhibit three zonally aligned maxima along 37°N between 140°E and 160°E (Fig. 5).
528 The projected RSL rise maxima during 2081–2100 relative to 1981–2000 reach 63, 67,
529 and 76 cm, in ROMS-MIROC, ROMS-CSIRO, and ROMS-GFDL, respectively (Fig.
530 5).

531 All ROMS downscaling commonly show that the coastal RSL rises are smaller
532 than the off-shore RSL rises (Figs. 5 and 8), consistent with Sato et al. (2006). The
533 projected RSL rises along the Honshu coast during 2081–2100 relative to 1981–2000
534 are 19–25, 6–15, and 8–14 cm in ROMS-MIROC, ROMS-CSIRO, and ROMS-GFDL,
535 respectively, which are generally half or less of the RSL rise maxima off the eastern
536 coast of Japan. Moreover, the ranges of RSL changes along the Honshu coast are small
537 in all ROMS downscaling, probably due to shelf waves, which play a role in spatial
538 averaging associated with wave's propagation along the coast (Fig. 9). Although the

539 CMIP5 models underestimate off-shore RSL rise maxima substantially than ROMS
540 downscaling (Figs. 5, 7, and 8), the discrepancies between the climate models and
541 ROMS downscaling are less than 10 cm along the Honshu coast (Fig. 9). Because the
542 averaging effects of the shelf waves do not contribute to the sea level for islands
543 separated from Honshu, larger RSL changes can occur for some islands than those along
544 Honshu with larger differences between the climate models and ROMS downscaling. At
545 Okinawa Island, the RSL changes are nearly 30 cm in ROMS-MIROC and
546 ROMS-CSIRO, which is higher than the changes along the Honshu coast. The
547 difference in RSL rise at Okinawa Island between ROMS-CSIRO and CSIRO-Mk3.6.0
548 exceeds 10 cm (Fig. 10).

549 In ROMS-GFDL, the RSL changes to the east of Japan are accompanied by the
550 zonal velocity changes across KE in the upper 1000 m, penetrating down to 2000 m
551 (Fig. 12), probably due to wind stress changes (e.g., Sakamoto et al. 2005; Sato et al.
552 2006; Sueyoshi and Yasuda 2012), whereas the shallow velocity and near surface
553 density changes in ROMS-CSIRO suggests that water mass changes play a larger role
554 than the other two models. Both the effects of wind stress and water mass changes are
555 likely to be included in ROMS-MIROC. The RDH changes relative to 2000 dbar
556 reproduce major features of RSL rises very well, including RSL rises associated with
557 the KE changes mainly contributed by the thermosteric component rather than from the
558 halosteric component (Fig. 11).

559 Other factors that are not taken into account in the present downscaling simulation
560 can influence RSL changes, such as the inverse barometer effect, glacial isostatic
561 adjustment (GIA), gravitational changes resulted from land ice melting and changes of
562 land water storage, and climate model drift (Church et al. 2013; Slangen et al. 2014).

563 The inverse barometer effect, which yields an absolute sea level change less than 3 cm
564 over the North Pacific in all models, is much smaller than the steric and land ice
565 contributions and hence can be neglected. Based on the IPCC AR5, the GIA and
566 gravitation changes has a relatively small effect around Japan. Climate drifts of the three
567 CMIP5 climate models, which are evaluated using the pre-industry control run, are
568 small for RSL in the western North Pacific, and can be ignored.

569 In order to obtain information useful for society, it is important to evaluate total sea
570 level rise, which can be obtained by the RSL change through downscaling and the
571 global mean sea level rise. Contributions to global mean sea level change include
572 glaciers, land ice and land water storage contributions, thermal expansion contribution,
573 and GIA (Church et al. 2013; Slangen et al. 2014). The GIA effect on the global mean
574 sea level is small (-3 cm in 100 years) (Peltier and Luthcke 2009). The glaciers, land ice,
575 and land water storage contributions to the global mean sea level rise are nearly 16, 16,
576 and 4 cm, respectively, in 2081–2100 relative to 1986–2005 for RCP8.5 in IPCC AR5
577 (Table 13.SM.1, Church et al. 2013). The thermal expansion components during 2081–
578 2100 relative to 1981–2000 under RCP8.5 are 43, 29, and 36 cm, in MIROC-ESM,
579 CSIRO-Mk3.6.0, and GFDL-CM3, respectively[1]. As a result, the global mean sea level
580 rise are 79, 65, and 72 cm during 2081–2100 relative to 1981–2000 under RCP8.5 in
581 MIROC-ESM, CSIRO-Mk3.6.0, and GFDL-CM3, as a minor reference period
582 difference of 20th century, i.e., 1986–2005 in AR5 and 1980–2000 in the present study,
583 can be ignored. Consequently, the coastal sea level rise in total, which is given by the

[1] Globally averaged sea-level due to thermal expansion (thermosteric component) is estimated with a variable, zostoga, in CMIP5. However, zostoga is not available for GFDL-CM3, and thus we use another variability, zossga, (global average steric sea level change). For MIROC-ESM, both zostoga and zossga are available and the difference between them are small (less than 0.3% for 100 year difference).

addition of the RSL increase documented in section 3.2 and the global mean sea level rise, are expected to be 101–108, 73–80, and 80–90 cm in MIROC-ESM, CSIRO-Mk3.6.0, and GFDL-CM3, respectively.

An important result in the present study is that the present downscaling reveals that the discrepancy along the Honshu coast between the CMIP5 climate models and corresponding ROMS downscaling is less than 10 cm. Thus, with 10 cm uncertainty, the RSL change along the Honshu coast can be directly evaluated from CMIP5 climate model outputs. This allows the coastal RSL rise to be evaluated with a larger number of climate models (nearly 40), and the probability of sea level changes to be evaluated considering the uncertainties among climate models.

At the eddy-permitting 0.25° × 0.25° resolution here, ROMS-Hist exhibits some bias, such as the overshoot of the Kuroshio Current and the northward shift of KE compared with observations. Although we have taken these biases into account in interpreting the downscaled sea level changes, it is not possible to identify the specific locations and magnitudes of the largest coastal sea level rise. To overcome these biases, downscaling with eddy-resolving resolution of 0.1° × 0.1° may be required. This should be an important research in future, because Tokyo, the most densely city and the capital of Japan, is located near from the separation point of the Kuroshio at 35°N. The computational cost of this resolution is about 16 times larger than that in our experiments, which we expect will become feasible for a number of laboratories in the next decade.

Acknowledgments

We thank for fruitful discussion with Dr. Tamaki Yasuda and Dr. Tatsuo Suzuki.

608 This work was supported by JSPS KAKENHI Grant Numbers 26287110, 26610146,
609 15H01606. The numerical calculations were carried out on a computer in the Institute of
610 Low Temperature Science, Hokkaido University.

611

612 ## References

613 Abdul-Aziz OI, Mantua NJ, Myers KW (2011) Potential climate change impacts on
614 thermal habitats of Pacific salmon (Oncorhynchus spp.) in the North Pacific Ocean
615 and adjacent seas. Can J Fish Aquat Sci 68(9):1660-1680. doi: 10.113/F2011-079

616 Ådlandsvik B (2008) Marine downscaling of a future climate scenario for the North Sea.
617 Tellus 60A:451-458. doi: 10.1111/j.1600-0870.2008.00311.x

618 Antonov JI, Seidov D, Boyer TP, Locarnini RA, Mishonov AV, Garcia HE, Baranova
619 OK, Zweng MM, Johnson DR (2010) World Ocean Atlas 2009. In: Levitus S (eds)
620 Vol. 2. Salinity, NOAA Atlas NESDIS 68, Government Printing Office, Washington,
621 pp. 184

622 Bindoff NL et al (2007) Observations: Oceanic climate change and sea level. In:
623 Solomon S et al (eds) Climate Change 2007: The Physical Science Basis.
624 Contribution of Working Group I to the Fourth Assessment Report of the
625 Intergovernmental Panel on Climate Change, Cambridge University Press,
626 Cambridge

627 Carton JA, Giese BS (2008) A reanalysis of ocean climate using Simple Ocean Data
628 Assimilation (SODA), Mon Weather Rev 136(8):2999-3017

629 Cazenave A, Cozannet GL (2013) Sea level rise and its coastal impacts. Earth's Future
630 2:15-34. doi: 10.1002/2013EF000188

631 Chamberlain MA, Sun CJ, Matear RJ, Feng M, Phipps SJ (2012) Downscaling the

632 climate change for oceans around Australia. Geosci Model Dev 5:1177-1194
633 Chelton DB, Xie SP (2010) Coupled ocean-atmosphere interaction at oceanic
634 mesoscales. Oceanog 23(4):52-69
635 Church JA et al (2013) Sea Level Change. In: Stocker TF et al (eds) Climate Change
636 2013: The Physical Science Basis. Contribution of Working Group I to the Fifth
637 Assessment Report of the Intergovernmental Panel on Climate Change, Cambridge
638 University Press, Cambridge
639 Curchitser EN, Haidvogel DB, Hermann AJ, Dobbins EL, Powell TM, Kaplan A (2005)
640 Multi-scale modeling of the North Pacific Ocean: Assessment and analysis of
641 simulated basin-scale variability (1996-2003). J Geophys Res 110(C11021). doi:
642 10.1029/2005JC002902
643 Ducet N, Le Traon PY, Reverdin G (2000) Global high resolution mapping of ocean
644 circulation from TOPEX/Poseidon and ERS-1/2. J Geophys Res 105(19):477-498
645 Fairall CW, Bradley EF, Hare JE, Grachev AA, Edson JB (2003) Bulk parameterization
646 of air-sea fluxes: Updates and verification for the COARE algorithm. J Clim
647 16:571-591
648 Fukamachi Y, Ohshima KI, Ebuchi N, Bando T, Ono K, Sano M (2010) Volume
649 transport in the Soya strait during 2006-2008. J Oceanogr 66:685-696
650 Fukudome K, Yoon JH, Ostrovskii A, Takikawa T, Han IS (2010) Seasonal volume
651 transport variation in the Tsushima warm current through the Tsushima Straits from
652 10 years of ADCP observations. J Oceanogr 66:539-551
653 Gill AE (1982) Atmosphere-ocean dynamics. Academic Press, Harcourt Place, London,
654 pp. 215
655 Griffies SM et al (2005) Formulation of an ocean model for global climate simulations.

656 Ocean Sci 1:45-79
657 Griffies SM, Winton M, Donner LJ et al (2011) The GFDL CM3 coupled climate
658 model: Characteristics of the ocean and sea ice simulations. J Clim 24:3520-3544.
659 doi: 10.1175/2011JCLI3964.1
660 Haidvogel DB, Arango HG, Hedstrom K, Beckmann A, Malanotte-Rizzoli P,
661 Shchepetkin AF (2000) Model evaluation experiments in the North Atlantic
662 basin:Simulations in nonlinear terrain-following coordinates. Dyn Atmos Oceans
663 32:239-281
664 Han W, Moore AM, Levin J, Zhang B, Arango HG, Curchitser E, Lorenzo ED, Gordon
665 AL, Lin J (2009) Seasonal surface ocean circulation and dynamics in the Philippine
666 Archipelago region during 2004-2008. Dyn Atmos Oceans 47:114-137
667 Hanson S, Nicholls R, Ranger N, Hallegatte S, Corfee-Morlot J, Herweijer C, Chateau J
668 (2011) A global ranking of port cities with high exposure to climate extremes. Clim
669 Change 104:89-111. doi: 10.1007/s10584-010-9977-4
670 Ito T, Togawa O, Ohnishi M, Isoda Y, Nakayama T, Shima S, Kuroda H, Iwahashi M,
671 Sato C (2003) Variation of velocity and volume transport of the Tsugaru warm
672 current in the winter of 1999-2000. Geophys Res Lett 30(13):1678.
673 doi:10.1029/2003GL017522
674 Jeffrey SJ, Rotstayn L, Collier M, Dravitzk S, Hamalaien C, Moeseneder C, Wong K,
675 Syktus J (2013) Australia's CMIP5 submission using the CSIRO Mk3.6 model.
676 Aust Meteorol Oceanogr J 63:1-13
677 Kagimoto T, Yamagata T (1997) Seasonal transport variations of the Kuroshio: An
678 OGCM simulation. J Phys Oceanogr 27:403-418.
679 Landerer FW, Jungclaus JH, Marotzke J (2007) Regional dynamic and steric sea level

680 change in response to the IPCC=A1B scenario. J Phys Oceanogr 37:296-312
681 Large WG, McWilliams JC, Doney SC (1994) Oceanic vertical mixing: A review and a
682 model with a nonlocal boundary layer parameterization. Rev Geophys 32:363-404
683 Large WG, Yeager S (2009) The global climatology of an interannually varying air-sea
684 flux data set. Clim Dyn 33:341-364. doi: 10.1007/s00382-008-0441-3
685 Lee T, Waliser DE, Li JF, Landerer FW, Gierach MM (2013) Evaluation of CMIP3 and
686 CMIP5 wind stress climatology using satellite measurements and atmospheric
687 reanalysis products. J Clim 26:5810-5826. doi: 10.1175/JCLI-D-12-00591.1
688 Liu Y, Xie L, Morrison JM, Kamykowski D (2013) Dynamic downscaling of the impact
689 of climate change on the ocean circulation in the Galápagos Archipelago. Adv
690 Meteorol 2013:1-18
691 Liu Y, Lee SK, Enfield DB, Muhling BA, Lamkin JT, Muller-Karger FE, Roffer MA
692 (2015) Potential impact of climate change on the Intra-Americas Sea: Part-1. A
693 dynamic downscaling of the CMIP5 model projections. J Mar Sys 148(2015):56-69
694 Liu Z, Wu L (1999) Rossby wave-coastal kelvin wave interaction in the extratropics.
695 part II: Formatioin of island circulation. J Phys Oceanogr 29:2405-2418
696 Locarnini RA, Mishonov AV, Antonov JI, Boyer TP, Garcia HE, Baranova OK, Zweng
697 MM, Johnson DR (2010) World Ocean Atlas 2009. In: Levitus S (eds) Vol. 1.
698 Temperature, NOAA Atlas NESDIS 68, Government Printing Office, Washington,
699 pp. 184
700 Lorenzo ED, Schneider N, Cobb KM Franks PJS, Chhak K et al (2008) North Pacific
701 gyre oscillation links ocean climate and ecosystem change. Geophys Res Lett
702 35(L08607)
703 Lowe JA, Gregory M (2006) Understanding projections of sea level rise in a Hadley

704 Centre coupled climate model. J Geophys Res 111(C11014). doi:
705 10.1029/2005JC003421
706 Lyu SJ, Kim K (2005) Subinertial to interannual transport variations in the Korea Strait
707 and their possible mechanisms. 110(C1206). doi: 10.1029/2004JC002651
708 Marchesiello P, McWilliams JC, Shchepetkin A (2001) Open boundary conditions for
709 long-term integration of regional oceanic model. Ocean Modell 3:1-20
710 Meier HEM (2006) Baltic Sea climate in the late twenty-first century: A dynamical
711 downscaling approach using two global models and two emission scenarios. Clim
712 Dyn 27(1):39-68. doi: 10.1007/s00382-006-0124-x
713 Moss RH, Edmonds JA, Hibbard KA et al (2010) The next generation of scenarios for
714 climate change research and assessment. Nature 463:747-756.
715 doi:10.1038/nature08823
716 Nicholls RJ, Hanson S, Herweijer C, Patmore N, Hallegatte S et al (2008) Ranking port
717 cities with high exposure and vulnerability to climate extremes: exposure estimates.
718 OECD Publishing. http://dx.doi.org/10.1787/011766488208
719 Ohshima KI (1994) The flow system in the Japan Sea caused by a sea level difference
720 through shallow straits. J Geophys Res 99:9925-9940
721 Oliver ECJ, Holbrook NJ (2014) Extending our understanding of South Pacific gyre
722 "spin-up": Modeling the East Australian Current in a future climate. J Geophys Res
723 Ocean 119:2788-2805. doi: 10.1002/2013JC009591
724 Peltier WR, Luthcke SB (2009) On the origins of Earth rotation anomalies: New
725 insights on the basis of both "paleogeodetic" data and Gravity Recovery and
726 Climate Experiment (GRACE) data. J Geophys Res 114(B11405).
727 doi:10.1029/2009JB006352

728 Rio MH, Hernandez F (2004) A mean dynamic topography computed over the world
729 ocean from altimetry, in situ measurements, and a geoid model. J Geophys Res
730 109(C12032). doi:10.1029/2003JC002226
731 Rotstayn LD et al (2010) Improved simulation of Australian climate and ENSO-related
732 rainfall variability in a global climate model with an interactive aerosol treatment.
733 Int J Climatol 30:1067-1088. doi: 10.1002/joc.1952
734 Sakamoto TT, Hasumi H, Ishii M, Emori S, Suzuki T, Nishimura T, Sumi A (2005)
735 Responses of the Kuroshio and the Kuroshio Extension to global warming in a
736 high-resolution climate model. Geophys Res Lett 32(L14617).
737 doi:10.1029/2005GL023384
738 Sasaki YN, Minobe S, Miura Y (2014) Decadal sea-level variability along the coast of
739 Japan in response to ocean circulation changes. J Geophys Res Oceans 119:266-275.
740 doi: 10.1002/2013JC009327
741 Sato Y, Yukimoto S, Tsujino H, Ishizaki H, Noda A (2006) Response of North Pacific
742 ocean circulation in a Kuroshio-resolving ocean model to an Arctic Oscillation
743 (AO)-like change in Northern Hemisphere atmospheric circulation due to
744 greenhouse-gas forcing. J Meteorol Soc Jpn 84:295-309
745 Sen Gupta A, Jourdain NC, Brown JN, Monselesan D (2013) Climate drift in the
746 CMIP5 models. J Clim 26:8597-8615. doi: 10.1175/JCLI-D-12-00521.1
747 Seo H, Miller AJ, Roads JO (2007) The scripps coupled ocean-atmosphere regional
748 (SCOAR) model, with applications in the eastern Pacific sector. J Clim 20:381-402
749 Seo GH, Cho YK, Choi BJ, Kim KY, Kim BG, Tak YJ (2014) Climate change
750 projection in the Northwest Pacific marginal seas through dynamic downscaling. J
751 Geophys Res Oceans 119:3497-3516. doi: 10.1002/2013JC009646

752 Shchepetkin AF, McWilliams JC (2005) The regional oceanic modeling system
753 (ROMS): A split-explicit, free-surface, topography-following-coordinate ocean
754 model. Ocean Modell 9:347-404
755 Shu Q, Qian FL, Song ZY, Yin XQ (2013) Acomparison of two global ocean-ice
756 coupled models with different horizontal resolutions. Acta Oceanol Sin 32(8):1-11
757 Small RJ, deSzoeke SP, Xie SP, O'Neill L, Seo H, Song Q, Cornillon P, Spall M,
758 Minobe S (2008) Air-sea interaction over ocean fronts and eddies. Dyn Atmos
759 Oceans 45:274-319. doi: 10.1016/j.dynatmoce.2008.01.001
760 Sueyoshi M, Yasuda T (2012) Inter-model variability of projected sea level changes in
761 the western North Pacific in CMIP3 coupled climate models. J Oceanogr
762 68:533-543. doi: 10.1007/s10872-012-0117-9
763 Sumata H, Hashioka T, Suzuki T, Yoshie N, Okunishi T, Aita MN, Sakamoto TT, Ishida
764 A, Okada N, Yamanaka Y (2010) Effect of eddy transport on the nutrient supply
765 into the euphotic zone simulated in an eddy-permitting ocean ecosystem model. J
766 Mar Sys 83(2010):67-87. doi:10.1016/j.jmarsys.2010.07.002
767 Sun CJ, Feng M, Matear RJ, Chamberlain MA, Craig P, Ridgway KR, Schiller A (2012)
768 Marine downscaling of a future climate scenario for Australian boundary currents. J
769 Clim 25(8):2947-2962. doi: 10.1175/JCLI-D-11-00159.1
770 Suzuki T, Ishii M (2011a) Regional distribution of sea level changes resulting from
771 enhanced greenhouse warming in the Model for Interdisciplinary Research on
772 Climate version 3.2. Geophys Res Lett 38(L02601). doi:10.1029/2010GL045693
773 Suzuki T, Ishii M (2011b) Long-term regional sea level changes due to variations in
774 water mass density during the period 1981-2007. Geophys Res Lett 38(L21604).
775 doi: 10.1029/2011GL049326

776 Tokeshi T, Yanagi T (2003) High sea level caused at Naha in Okinawa Island. Oceanogr
777 Japan 12(4):395-405 (**in Japanese with English abstract**)
778 Tsujino H, Nakano H, Motoi T (2008) Mechanism of currents through the straits of the
779 Japan Sea: Mean state and seasonal variation. J Oceanogr 64:141-161
780 Watanabe S, Hajima T, Sudo K et al (2011) MIROC-ESM 2010: model description and
781 basic results of CMIP5-20c3m experiments. Geosci Model Dev 4:845-872.
782 doi:10.5194/gmd-4-845-2011
783 Yin J, Griffies SM, Stouffer RJ (2010) Spatial variability of sea level rise in twenty-first
784 century projections. J Clim 23:4585-4607. doi:10.1175/2010JCLI3533.1
785 Yin J (2012) Century to multi-century sea level rise projections from CMIP5 models.
786 Geophys. Res Lett 39(L17709). doi:10.1029/2012GL052947
787 Zhang XB, Church JA, Platten SM, Monselesan D (2014) Projection of subtropical gyre
788 circulation and associated sea level changes in the Pacific based on CMIP3 climate
789 models. Clim Dyn 43:131-144. doi:10.1007/s00382-013-1902-x
790
791
792
793
794
795
796
797
798
799

Figure Captions

Fig. 1 Projected RSL rises averaged over a domain bounded by 25°–40°N and 125°–180°E during 2081–2100 relative to 1981–2000 for 33 CMIP5 climate models. The three selected models are highlighted in red

Fig. 2 Topography around Japan from ROMS. Contours indicate bathymetric depths in meters, and gray areas indicate the land mask. Blue lines denote the locations of the Tsushima, Tsugaru, and Soya Straits. Red dots denote the costal stations used in Figure 9 and the Okinawa Island station (26.75°N, 128°E) in Figure 10

Fig. 3 Time-mean surface velocities (colors) and vector velocities (vectors) for 1993–2000 in the three selected CMIP5 climate models (a–c), the ROMS historical run (d), and the satellite-derived surface geostrophic currents (e)

Fig. 4 Time-mean RSL for 1993–2000 period in three CMIP5 climate models (a–c), the ROMS historical run (d), and the satellite observations (e)

Fig. 5 Projected changes in mean RSL around Japan for 2081–2100 relative to 1981–2000 in (left) CMIP5 climate models under the RCP8.5 scenario and in (right) ROMS downscaling simulations. Top, middle, and bottom panels are for MIROC-ESM, CSIRO-Mk3.6.0, and GFDL-CM3, respectively

824

825 Fig. 6 Time-mean surface absolute velocities (colors) and vector velocities (vectors)
826 averaged over 2081–2100 in (a) ROMS-MIROC, (b) ROMS-CSIRO, and (c)
827 ROMS-GFDL

828

829 Fig. 7 (top) RSL zonally averaged from 145°E to 155°E and temporally averaged for
830 1981–2000 (blue) and 2081–2100 (red), and (bottom) projected RSL rise zonally
831 averaged from 145° to 155°E (black) and projected Japanese eastern coastal RSL rise
832 (purple) for 2081–2100 relative to 1981–2000 in (left) MIROC-ESM, (middle)
833 CSIRO-Mk3.6.0, and (right) GFDL-CM3

834

835 Fig. 8 (top) RSL zonally averaged from 145°E to 155°E and temporally averaged for
836 1981–2000 (blue) and 2081–2100 (red), and (bottom) projected RSL rise zonally
837 averaged from 145° to 155°E (black) and projected Japanese eastern coastal RSL rise
838 (purple) for 2081–2100 relative to 1981–2000 for the ROMS downscaling simulations
839 with (left) ROMS-MIROC, (middle) ROMS-CSIRO, and (right) ROMS-GFDL

840

841 Fig. 9 Projected Japanese eastern (a) and western (b) coastal RSL rise for 2081–2100
842 relative to 1981–2000 in three CMIP5 models (triangles) and from ROMS simulations
843 (dots), with MIROC-ESM and ROMS-MIROC (blue), CSIRO-Mk3.6.0 and
844 ROMS-CSIRO (purple), and GFDL-CM3 and ROMS-GFDL (green). The labels A–D
845 and A'–D' correspond to the location of the red dots shown in Fig. 2

846

847 Fig. 10 Projected RSL rise (in centimeters) at Okinawa Island (26.75°N, 128°E, as

848 shown in Fig. 2) during 2081–2100 relative to 1981–2000 in MIROC-ESM,
849 CSIRO-Mk3.6.0, and GFDL-CM3 (black bars), and in the corresponding ROMS
850 downscaling simulations (blue bars)
851
852 Fig. 11 (a–c) RDH changes with reference to 2000 dbar during 2081–2100 relative to
853 the 1981–2000 period, (d–f) RDH changes due to the thermosteric component, and (g–i)
854 RDH changes due to halosteric components, and (j–l) the sum of the thermosteric and
855 halosteric components, in (left) ROMS-MIROC, (middle) ROMS-CSIRO, and (right)
856 ROMS-GFDL
857
858 Fig. 12 Projected changes in mean eastward velocity zonally averaged from 145°E
859 to155°E for 2081–2100 relative to 1981–2000 (colors) in (a) ROMS-MIROC, (b)
860 ROMS-CSIRO, and (c) ROMS-GFDL. Contours show the mean distribution for 1981–
861 2000. The contour interval is 0.05 m/s
862
863 Fig. 13 Projected changes in potential temperature (in °C, color shading, meridional
864 average has been removed at each depth) zonally averaged from 145°E to 155°E for
865 2081–2100 relative to 1981–2000 in (a) ROMS-MIROC, (b) ROMS-CSIRO, and (c)
866 ROMS-GFDL along with their mean value for 1981–2000 (contours). The contour
867 interval is 3°C
868
869 Fig. 14 Projected changes in Sverdrup stream function (Sv, color shading) for 2081–
870 2100 period relative to 1981–2000 period along with their mean value for 1981–2000
871 (contours) in (a) ROMS-MIROC, (b) ROMS-CSIRO, and (c) ROMS-GFDL. Contours

872 interval is 15Sv

873

874 Fig. 15 Time-mean volume transports (in Sv) through (a) Tsushima, (b) Tsugaru, and (c)
875 Sōya Strait for 1981–2000 (black) and 2081–2100 (blue) simulated by ROMS
876 downscaling

877

878 Fig. 16 Projected SST change (°C) for 2081–2100 and 1981–2000 in (top) the CMIP5
879 models and in (bottom) ROMS downscaling simulations for (left) MIROC-ESM,
880 (middle) CSIRO-Mk3.6.0, and (right) GFDL-CM3, respectively

881

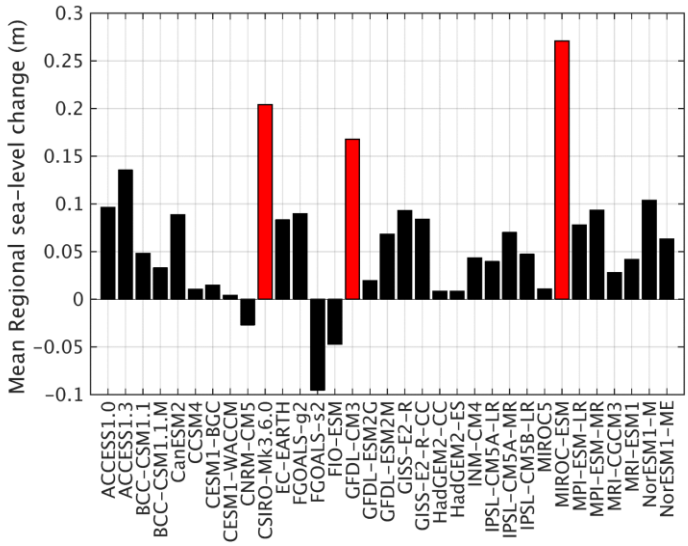

Fig. 1 Projected RSL rises averaged over a domain bounded by 25°–40°N and 125°–180°E during 2081–2100 relative to 1981–2000 for 33 CMIP5 climate models. The three selected models are highlighted in red.

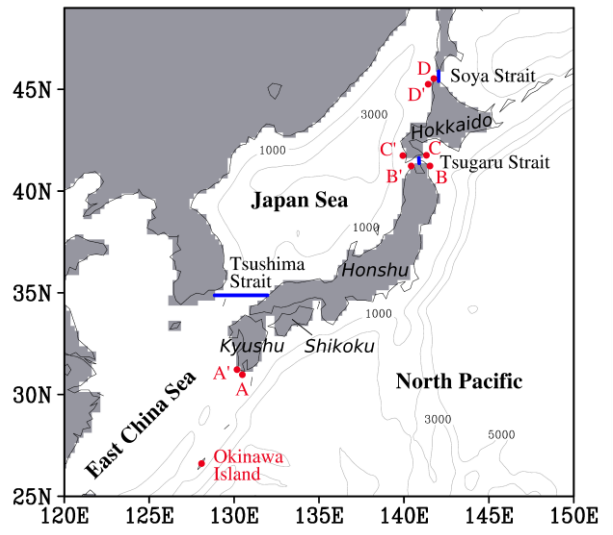

Fig. 2 Topography around Japan from ROMS. Contours indicate bathymetric depths in meters, and gray areas indicate the land mask. Blue lines denote the locations of the Tsushima, Tsugaru, and Soya Straits. Red dots denote the costal stations used in Figure 9 and the Okinawa Island station (26.75°N, 128°E) in Figure 10.

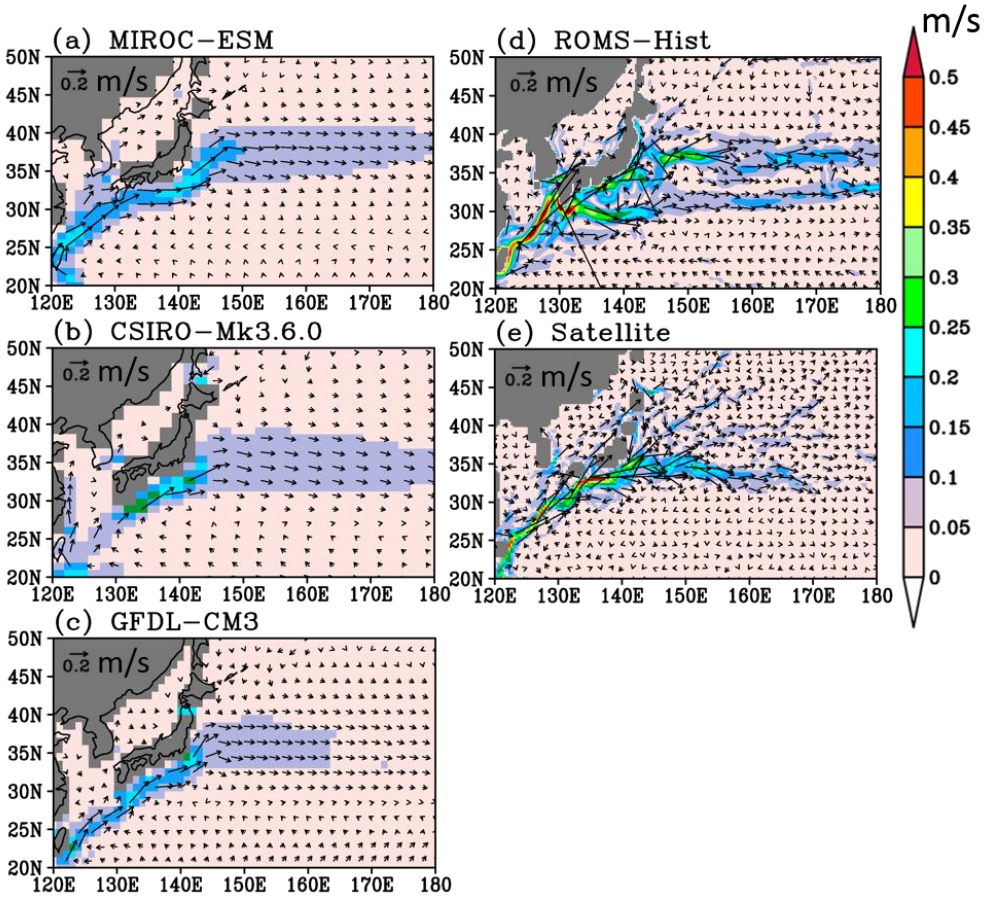

Fig. 3 Time-mean surface velocities (colors) and vector velocities (vectors) for 1993–2000 in the three selected CMIP5 climate models (a–c), the ROMS historical run (d), and the satellite-derived surface geostrophic currents (e).

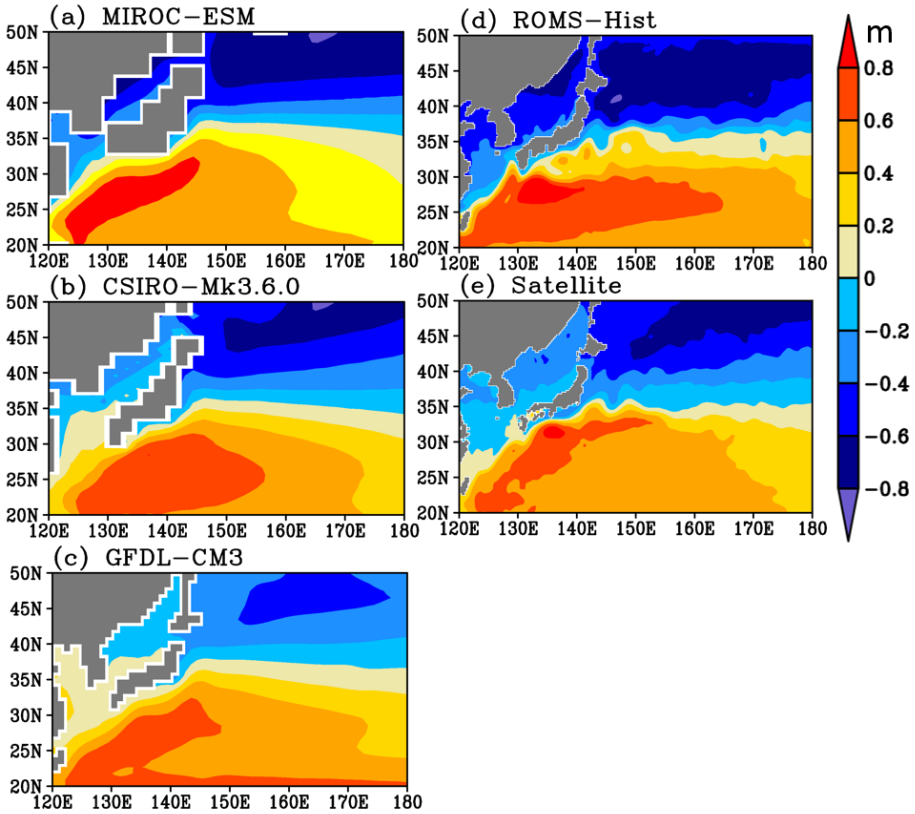

Fig. 4 Time-mean RSL for 1993–2000 period in three CMIP5 climate models (a–c), the ROMS historical run (d), and the satellite observations (e).

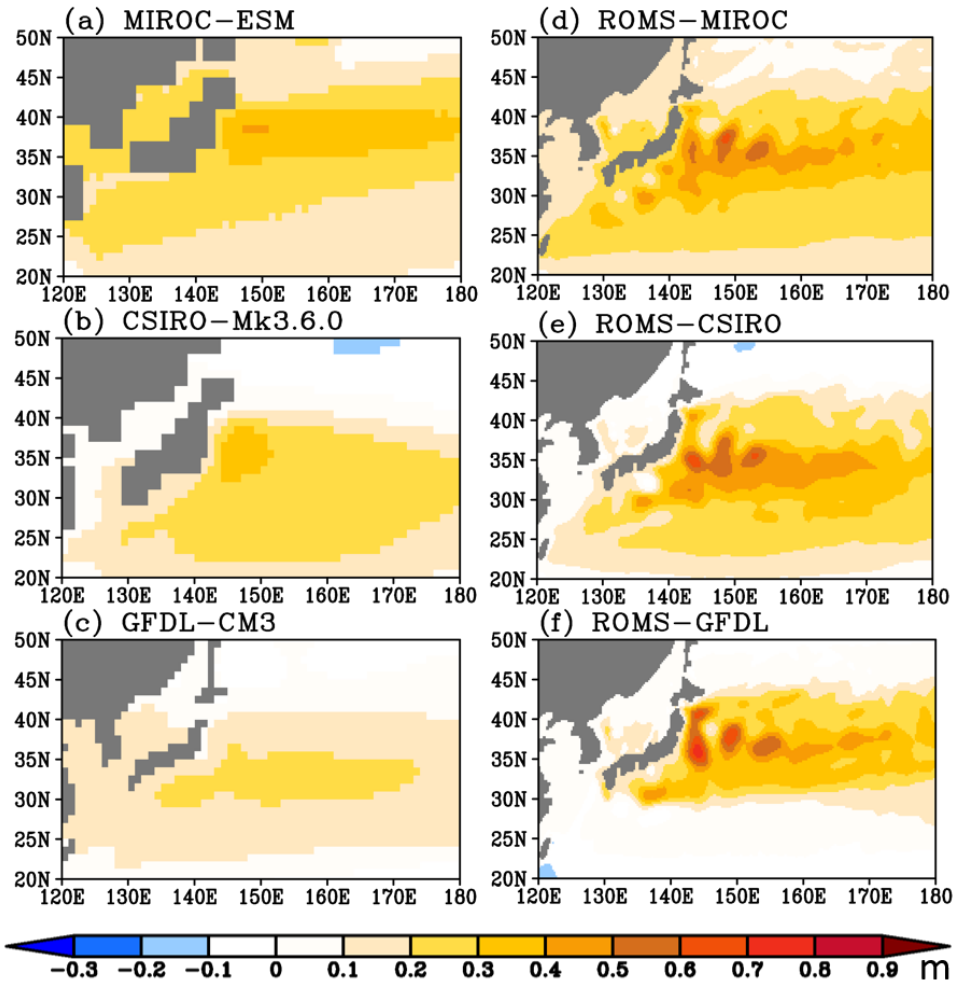

Fig. 5 Projected changes in mean RSL around Japan for 2081–2100 relative to 1981–2000 in (left) CMIP5 climate models under the RCP8.5 scenario and in (right) ROMS downscaling simulations. Top, middle, and bottom panels are for MIROC-ESM, CSIRO-Mk3.6.0, and GFDL-CM3, respectively.

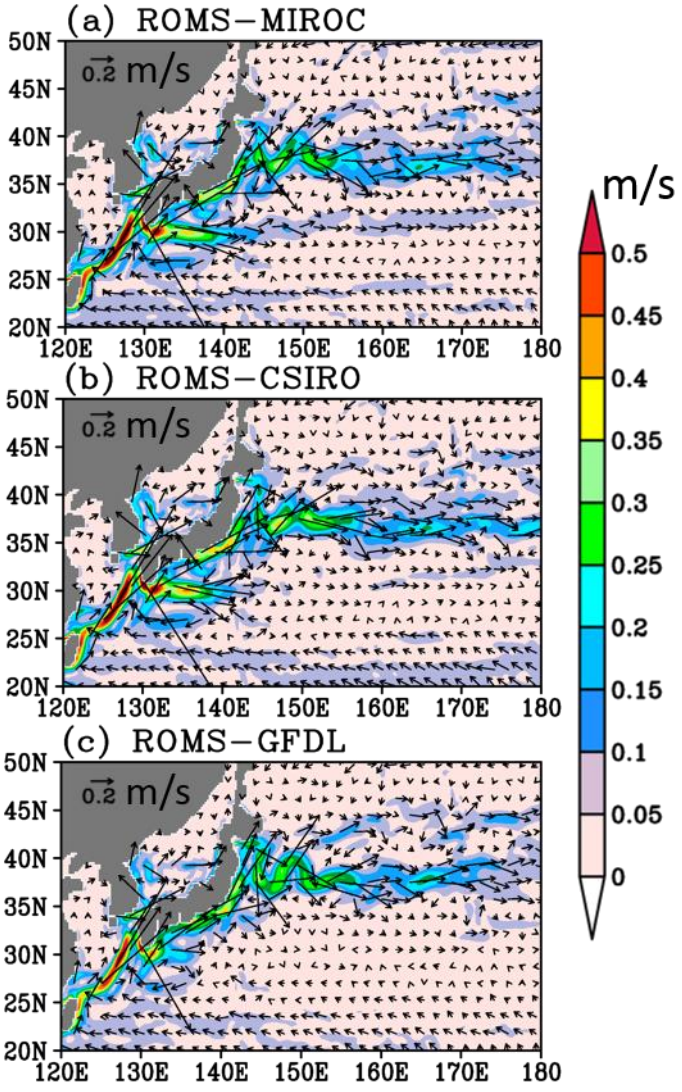

Fig. 6 Time-mean surface absolute velocities (colors) and vector velocities (vectors) averaged over 2081–2100 in (a) ROMS-MIROC, (b) ROMS-CSIRO, and (c) ROMS-GFDL.

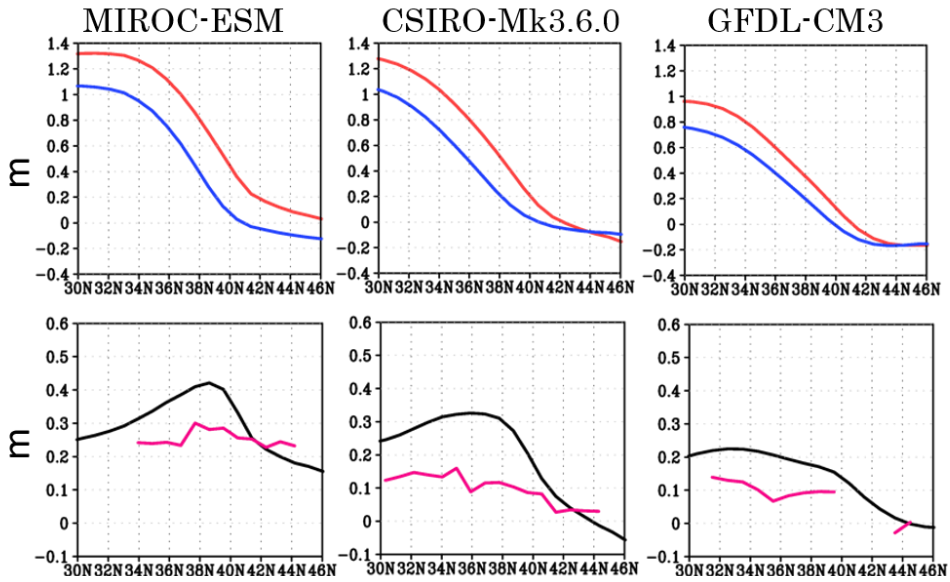

Fig. 7 (top) RSL zonally averaged from 145°E to 155°E and temporally averaged for 1981–2000 (blue) and 2081–2100 (red), and (bottom) projected RSL rise zonally averaged from 145° to 155°E (black) and projected Japanese eastern coastal RSL rise (purple) for 2081–2100 relative to 1981–2000 in (left) MIROC-ESM, (middle) CSIRO-Mk3.6.0, and (right) GFDL-CM3.

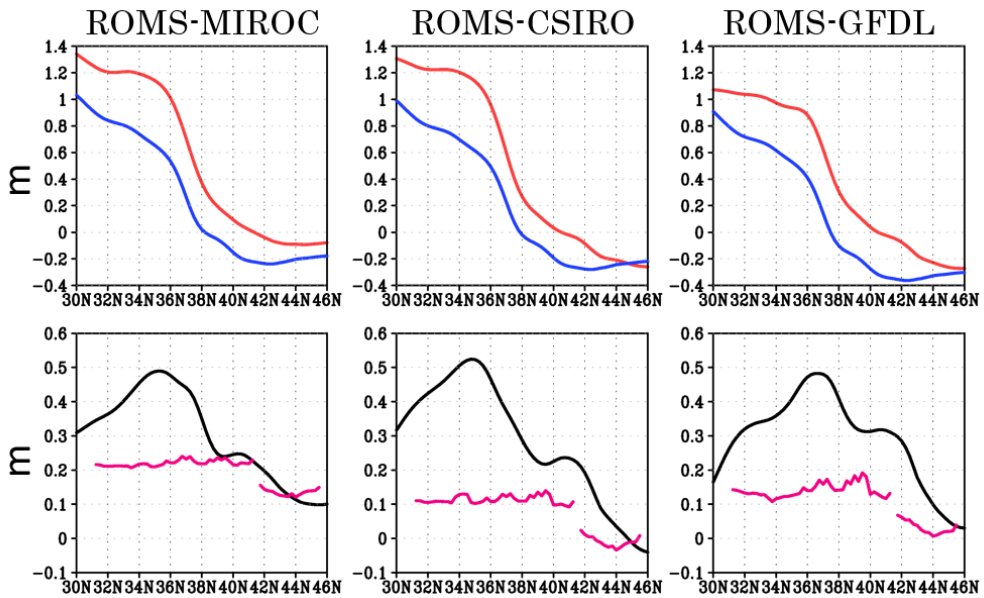

Fig. 8 (top) RSL zonally averaged from 145°E to 155°E and temporally averaged for 1981–2000 (blue) and 2081–2100 (red), and (bottom) projected RSL rise zonally averaged from 145° to 155°E (black) and projected Japanese eastern coastal RSL rise (purple) for 2081–2100 relative to 1981–2000 for the ROMS downscaling simulations with (left) ROMS-MIROC, (middle) ROMS-CSIRO, and (right) ROMS-GFDL.

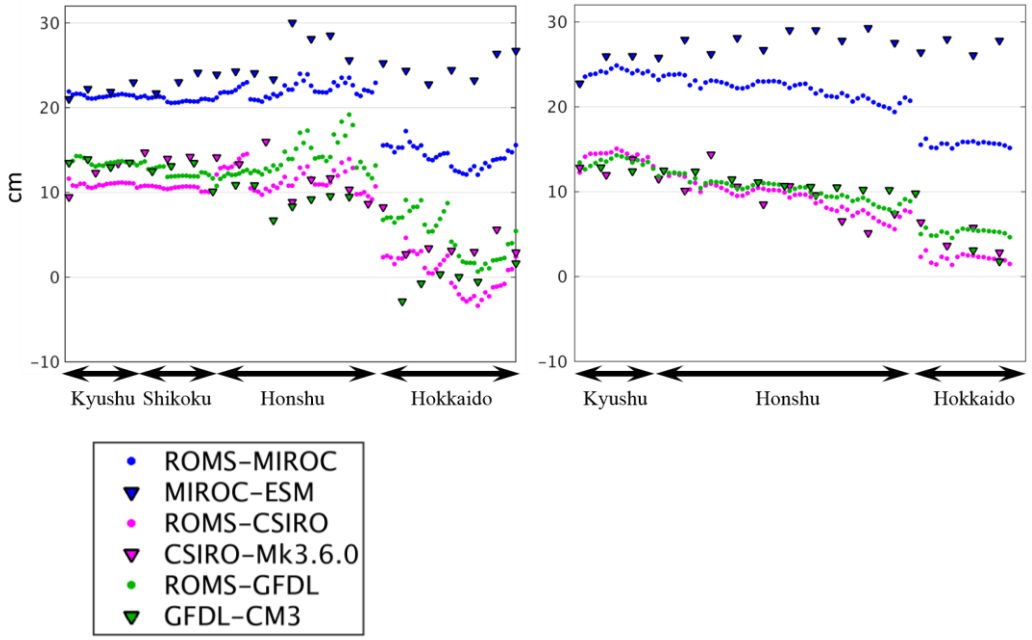

Fig. 9 Projected Japanese eastern (a) and western (b) coastal RSL rise for 2081–2100 relative to 1981–2000 in three CMIP5 models (triangles) and from ROMS simulations (dots), with MIROC-ESM and ROMS-MIROC (blue), CSIRO-Mk3.6.0 and ROMS-CSIRO (purple), and GFDL-CM3 and ROMS-GFDL (green). The labels A–D and A'–D' correspond to the location of the red dots shown in Fig. 2.

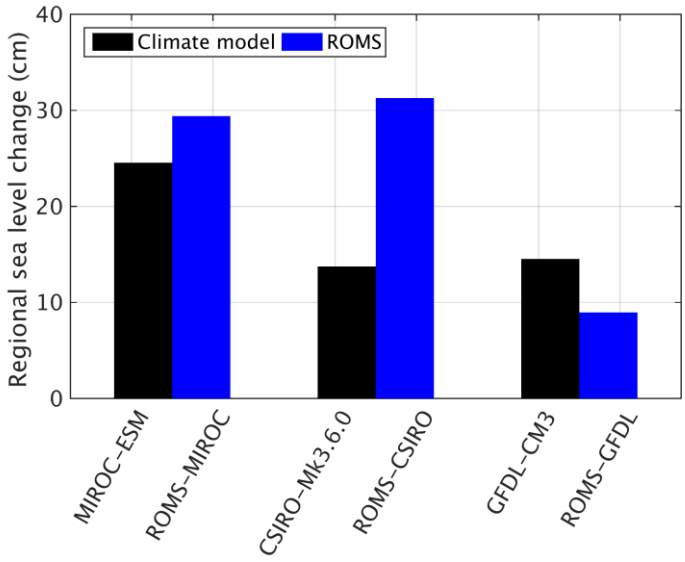

Fig. 10 Projected RSL rise (in centimeters) at Okinawa Island (26.75°N, 128°E, as shown in Fig. 2) during 2081–2100 relative to 1981–2000 in MIROC-ESM, CSIRO-Mk3.6.0, and GFDL-CM3 (black bars), and in the corresponding ROMS downscaling simulations (blue bars).

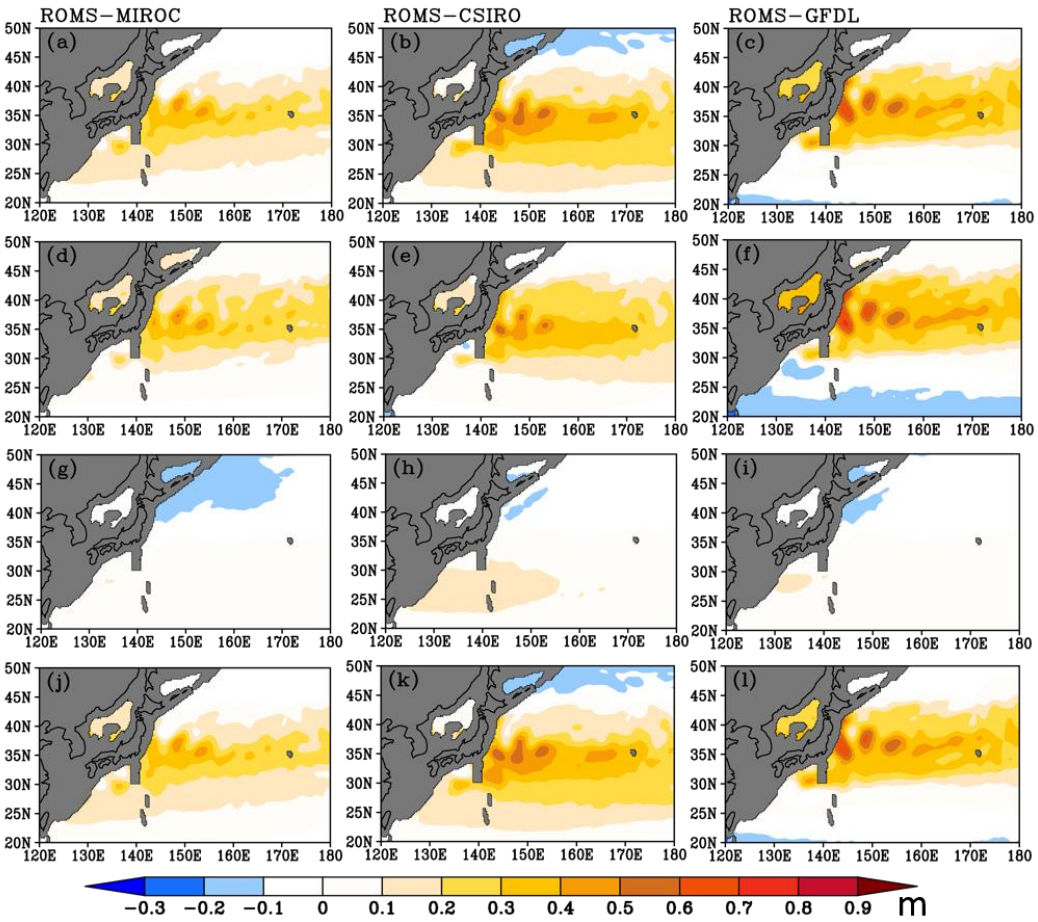

Fig. 11 (a–c) RDH changes with reference to 2000 dbar during 2081–2100 relative to the 1981–2000 period, (d–f) RDH changes due to the thermosteric component, and (g–i) RDH changes due to halosteric components, and (j–l) the sum of the thermosteric and halosteric components, in (left) ROMS-MIROC, (middle) ROMS-CSIRO, and (right) ROMS-GFDL.

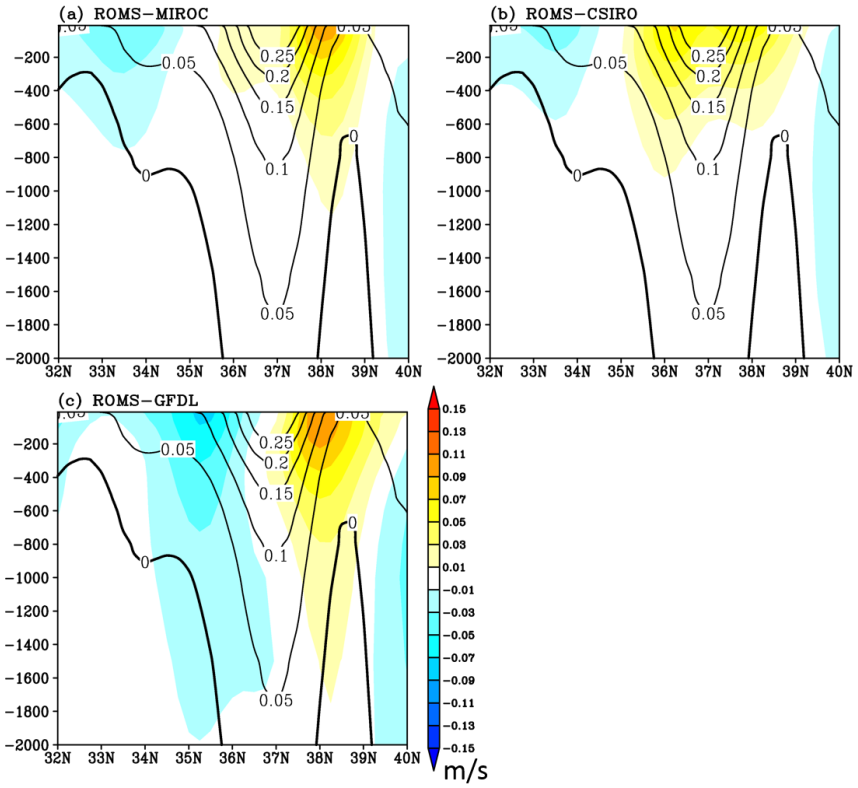

Fig. 12 Projected changes in mean eastward velocity zonally averaged from 145°E to155°E for 2081–2100 relative to 1981–2000 (colors) in (a) ROMS-MIROC, (b) ROMS-CSIRO, and (c) ROMS-GFDL. Contours show the mean distribution for 1981–2000. The contour interval is 0.05 m/s.

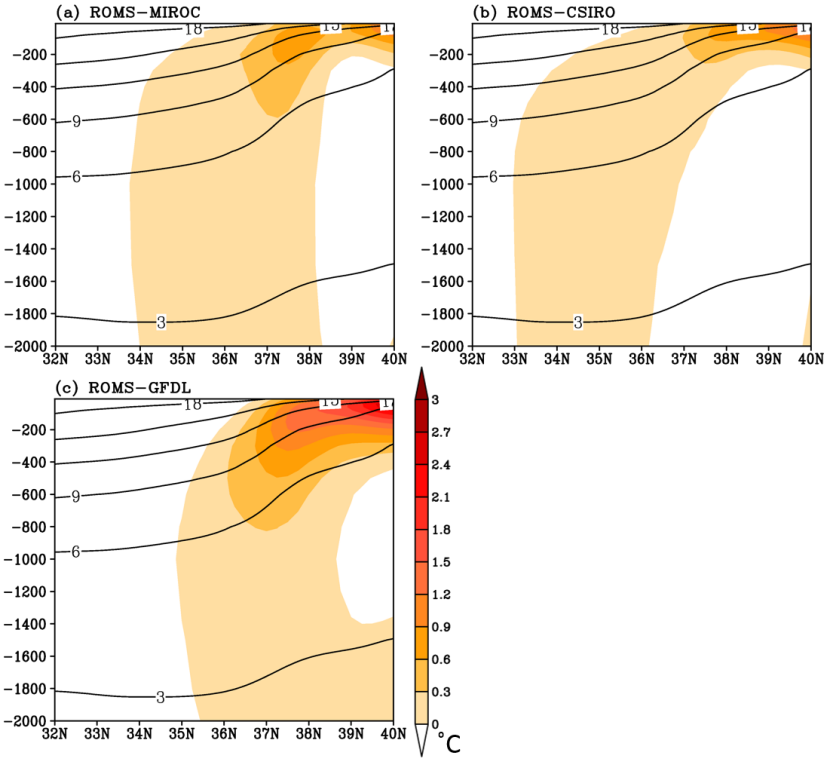

Fig. 13 Projected changes in potential temperature (in °C, color shading, meridional average has been removed at each depth) zonally averaged from 145°E to 155°E for 2081–2100 relative to 1981–2000 in (a) ROMS-MIROC, (b) ROMS-CSIRO, and (c) ROMS-GFDL along with their mean value for 1981–2000 (contours). The contour interval is 3 °C.

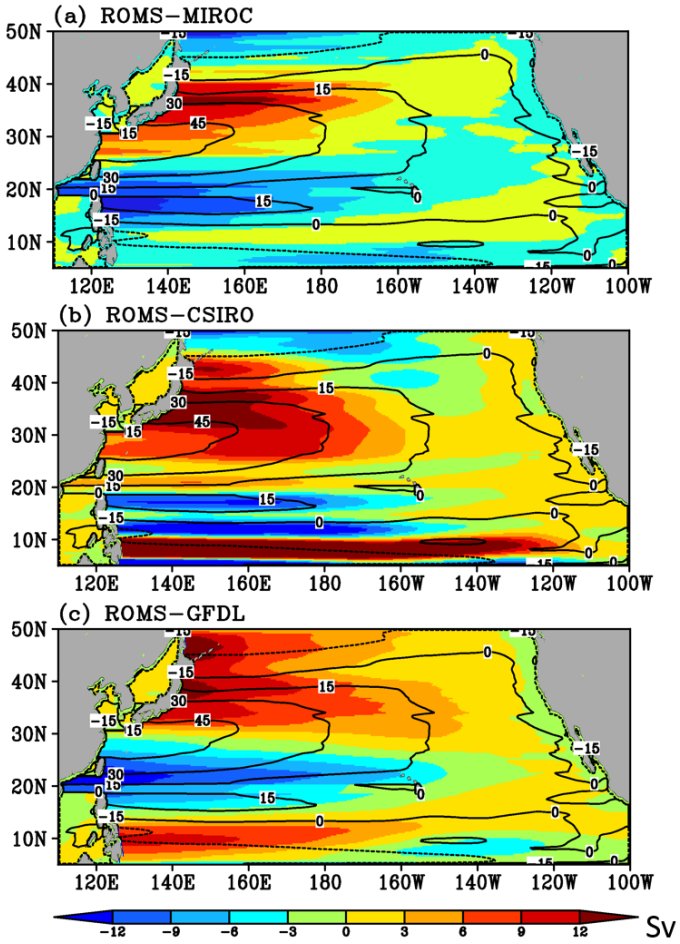

Fig. 14 Projected changes in Sverdrup stream function (Sv, color shading) for 2081–2100 period relative to 1981–2000 period along with their mean value for 1981–2000 (contours) in (a) ROMS-MIROC, (b) ROMS-CSIRO, and (c) ROMS-GFDL. Contours interval is 15Sv.

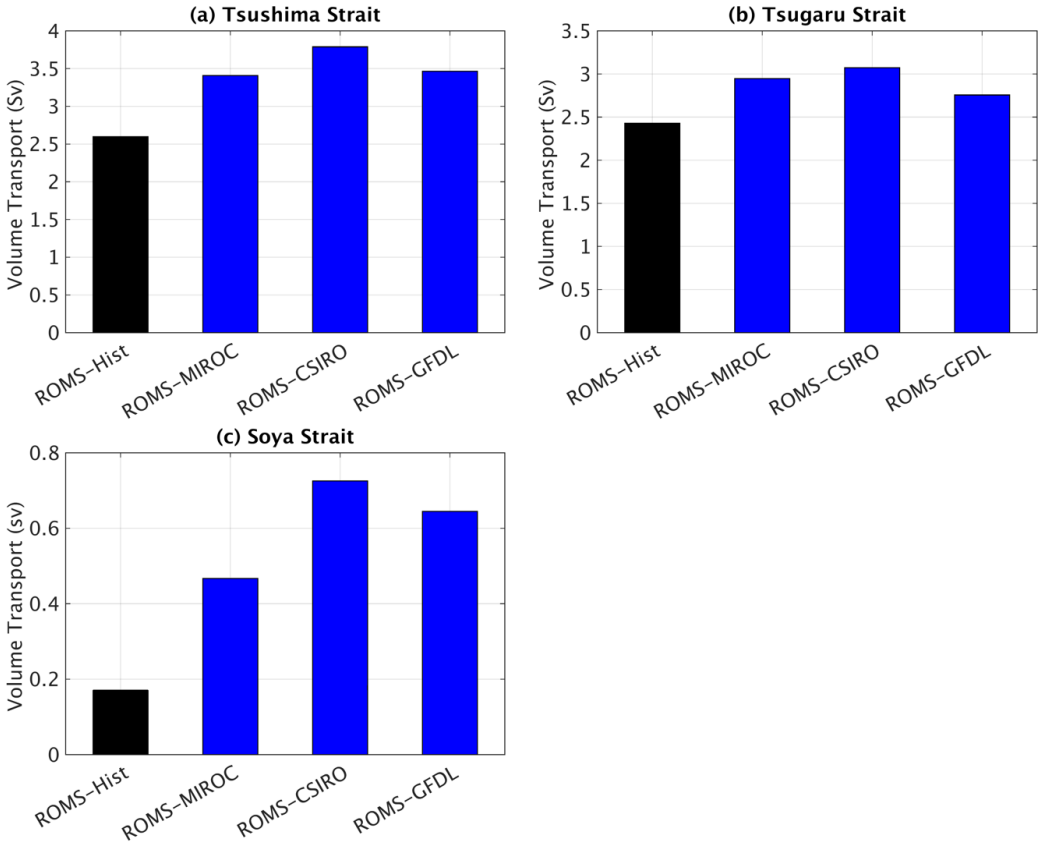

Fig. 15 Time-mean volume transports (in Sv) through (a) Tsushima, (b) Tsugaru, and (c) Sōya Strait for 1981–2000 (black) and 2081–2100 (blue) simulated by ROMS downscaling.

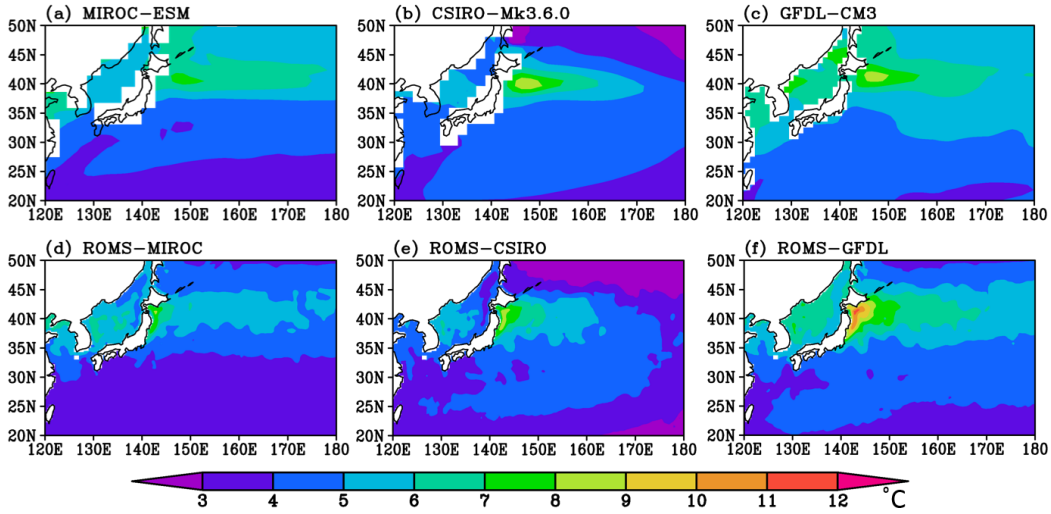

Fig. 16 Projected SST change (°C) for 2081–2100 and 1981–2000 in (top) the CMIP5 models and in (bottom) ROMS downscaling simulations for (left) MIROC-ESM, (middle) CSIRO-Mk3.6.0, and (right) GFDL-CM3, respectively.